

## Clouds and Precipitation

### Retrieved Vertical Profiles of Latent Heat Release Using TRMM Rainfall Products

Rainfall is a key link in the hydrologic cycle and is a primary heat source that fuels the general circulation of the atmosphere. The vertical distribution of latent heat release, which is accompanied by rainfall, modulates the large-scale circulation of the tropics and in turn can affect mid-latitude weather. This latent heat release is a consequence of phase changes between vapor, liquid, and solid water. Present large-scale weather and climate models can simulate cloud latent heat release only crudely, thus reducing their confidence in predictions on both global and regional scales.

Laboratory scientists were the first to use NASA Tropical Rainfall Measuring Mission (TRMM) rainfall information to estimate the four-dimensional structure of latent heating on a global scale. We retrieved latent heating for 1 month (February 1998) over the global tropics, the coverage of the TRMM satellite. Figure 6-34 shows monthly mean latent heating at three different altitudes (2, 5 and 8 km) over the global tropics from the Goddard Convective-Stratiform (CSH) heating algorithm (developed by the Goddard mesoscale modeling group). The horizontal pattern of latent heat release coincides with areas of major convective activity such as the intertropical convergence zone (ITCZ) in the Pacific and Atlantic basins, the South Pacific Convergence Zone (SPCZ), and broad areas of precipitation events spread over the continental regions.

Heavy surface precipitation is associated with intense latent heating in the middle and upper troposphere. Upper tropospheric heating over the Pacific and Indian Oceans is much stronger than over Africa, South America, and the Atlantic Ocean. Higher stratiform amounts always contribute to higher maximum latent heating levels. Whether the higher stratiform proportions and more frequent vigorous convective events in the Pacific are related to the warmer SSTs needs to be studied using multiseason and multiyear retrieved latent heating profiles. Note that differential heating between the continents and oceans in the upper troposphere could generate strong horizontal gradients in the thermodynamic fields and could interact with the global circulation.

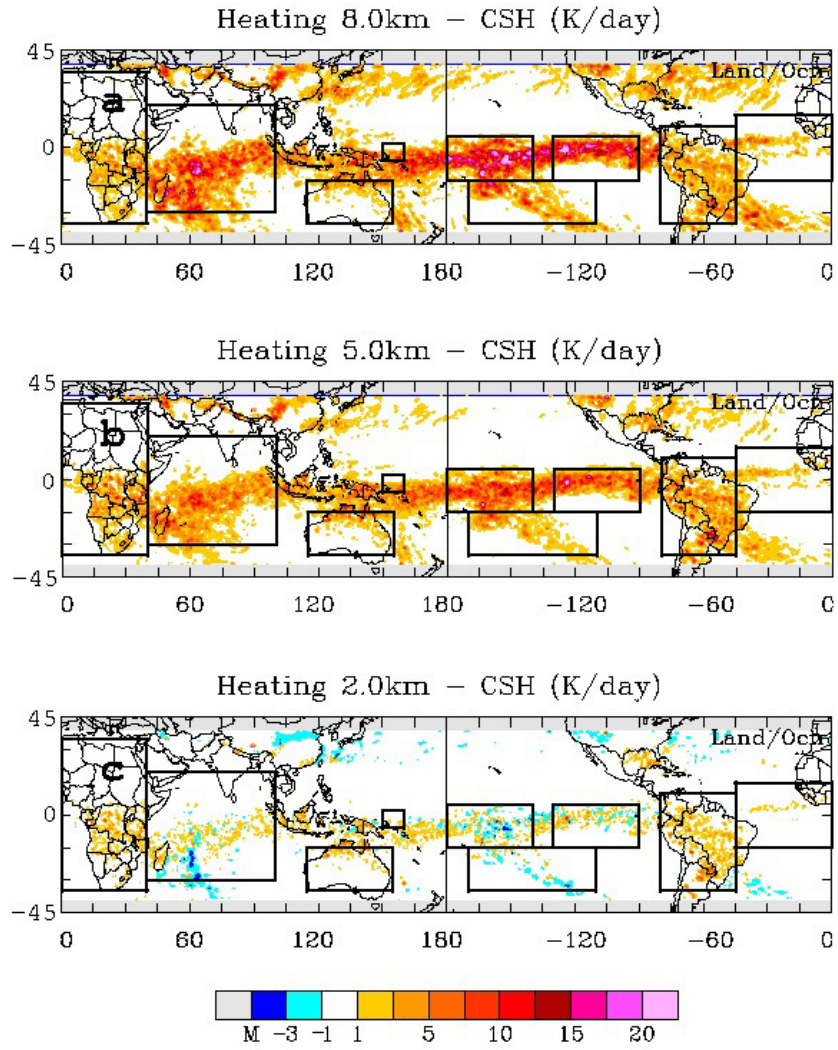


Figure 6-34. Monthly mean latent heating at 8, 5, and 2 km AGL over the global tropics derived from the Goddard Convective-Stratiform Heating (CSH) algorithm.

An interesting result from Figure 6-34 is the relatively strong cooling at 2 km over the Pacific (East, Central, and South) and Indian Oceans but not over Africa and South America. This result is unexpected, as the moisture content is higher over oceans. Cooling from rain evaporation in the lower troposphere should be stronger over drier areas. Several previous observational studies diagnosed the heating budgets from sounding networks located over the west Pacific warm pool region and the Amazon basin. The sounding budget showed weak, low-level cooling in the mean heating profile over the Pacific warm pool region for the month of February 1993. This cooling was induced by mesoscale downdrafts or evaporation by shallow cumuli. Observations also revealed that the relative humidity tended to be relatively low in the lower troposphere over the warm pool region. This would allow for more evaporative cooling. Budget results from the Amazon region did not exhibit low-level diabatic cooling. It has been suggested that the lowermost 2–3 km above the canopy of the Amazon rain forest is characterized by a strong diurnal cycle of evapotranspiration and upward convective fluxes of moisture, producing very large mixing ratios. The high moisture content during the wet season in the lower troposphere of the Amazon Basin may prevent or severely limit cooling below the cloud base. This indirect validation provides some confidence in our TRMM latent heating product. We are currently in the process of producing a multiyear latent heating data set using TRMM rainfall products.

Two other latent heating retrieval algorithms, the Goddard Profiling (GPROF) heating and the Hydrometeor heating (HH), were also used to estimate latent heating for February 1998. Their results were compared to those from the CSH algorithm. All three algorithms showed the same horizontal distribution pattern coincident with the major areas of convective activity in the tropics. The magnitudes of their estimated latent heating also agreed well with each other and with that determined from diagnostic budget studies. The major difference among the three algorithms was in the altitude of the retrieved maximum heating level. The latent heating profiles derived from the Goddard CSH heating algorithm agreed better with observations.

Two global climate models, from Goddard's DAO and from Florida State University, are currently using these data sets either to improve their cumulus parameterization schemes or to identify the problem in their parameterization schemes. Preliminary results indicate that these two global models have improved their energy and water cycles and their ability to forecast rainfall.

Wei-Kuo Tao, Code 912 ([Wei-Kuo.Tao.1@gsfc.nasa.gov](mailto:Wei-Kuo.Tao.1@gsfc.nasa.gov))

#### The Effects of Amazon Deforestation on Rainfall

This study began with the hypothesis that heavily deforested regions will experience increased surface heating, leading to local circulations that will ultimately *enhance* the rainfall. This would be an important finding because several modeling studies have concluded that widespread deforestation would lead to *decreased* rainfall. Toward that end, we analyzed rain estimates from a combined GOES infrared/TRMM microwave technique with respect to percent forest cover from Landsat data (courtesy of TRFIC at Michigan State University).

Figure 6-35 shows the area of interest in Rondonia (southwest Brazil). Five 1° x 1° areas of varying forest cover were examined during the “dry” season in Amazonia (July–Sept, 2000), when the effects of the surface would not be dominated by large-scale synoptic weather patterns.

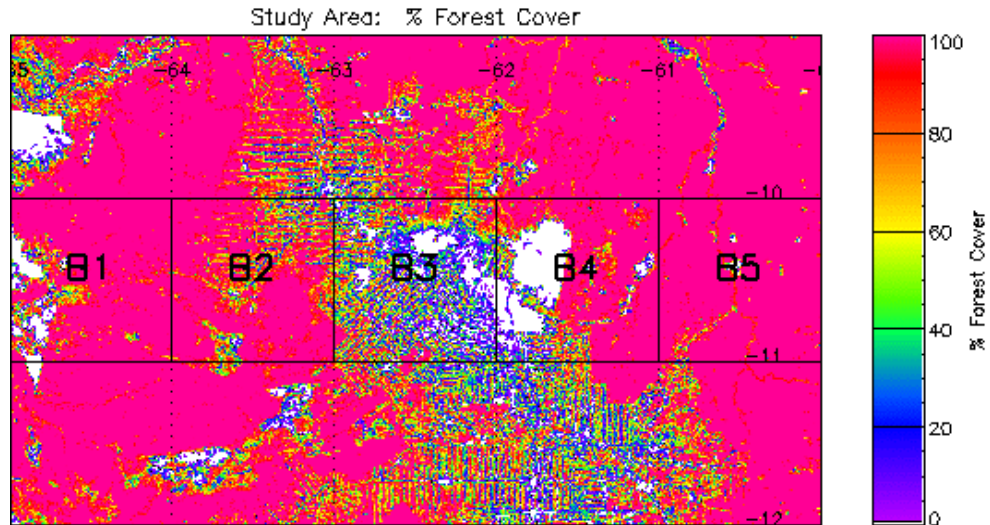


Figure 6-35. Five 1° x 1° areas of varying forest cover in Rondonia, southwest Brazil.

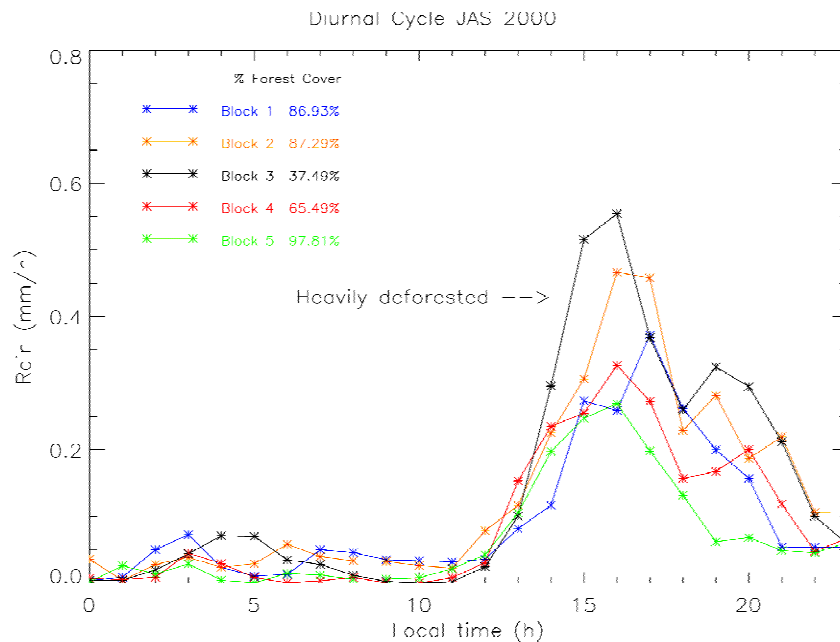


Figure 6-36. Rainfall amounts in the five regions versus local time.

Figure 6-36 presents results that show—

- Maximum rainfall fell in most deforested area (B3).
- Heavily forested areas (B1 and B5) received the least rainfall.
- Cloud development initiated at borders, and the diurnal cycle of precipitation may be a function of the surface cover.

These results should be viewed as preliminary, as only one season was examined and the error bars on the rain estimates are large.

Andrew J. Negri, Code 912 ([Andrew.J.Negri.1@gssc.nasa.gov](mailto:Andrew.J.Negri.1@gssc.nasa.gov))

### Sampling of the Diurnal Cycle of Precipitation using TRMM

One of the priority science questions in the design of the Tropical Rainfall Measuring Mission (TRMM) was “What is the diurnal (daily) cycle of tropical rainfall and how does it vary in space?” To answer this question, TRMM’s orbit was designed to precess (or make a complete cycle) through the 24 hours of the day during a period of 46 days. We have recently analyzed TRMM data to determine the optimal time period over which to accumulate the rainfall observations.

TRMM’s sampling pattern affects our ability to understand the daily variation of the rainfall estimates produced by the satellite’s two main instruments. These two instruments are the TRMM Microwave Imager (TMI) and Precipitation Radar (PR). These instruments have ground-track widths of 720 km and 220 km respectively. The combination of a long precession period and narrow ground-track results in peculiar patterns of sampling (the number of observations of any spot on the Earth).

Figure 6-37 shows the results from 3 years (1998–2000) of PR sampling at 1 hour of local time (00–01 LT). (The color scale highlights tropical sampling at the expense of the higher latitudes.) Note the absence of PR data over Australia due to an intergovernmental agreement. A checkerboard pattern in the hourly sampling at low latitudes is apparent. This pattern is examined in greater detail over a representative tropical region, the Amazon Basin (0–10° S, 75–50° W).

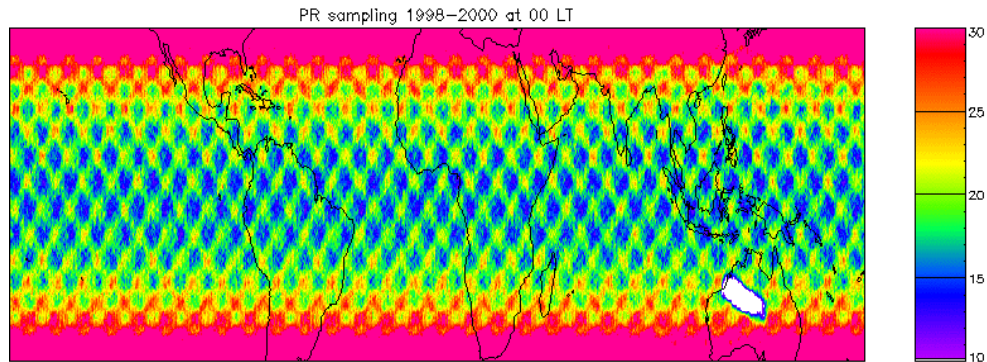


**Figure 6-37. Observed Precipitation Radar sampling at 00 Local Time (1998-2000).**

Figure 6-38 shows the PR sampling accumulated for periods from 1 to 6 h (plotted vertically) and for 1 year (2000) and 3 years (1998–2000) (plotted horizontally). The parameter  $\sigma/m$  is the standard deviation ( $\sigma$ ) divided by the mean ( $m$ ) of the grid cells in each scene. This ratio attempts to quantify the homogeneity of each scene, with lower numbers indicating more uniform sampling. It is evident that 4-hour accumulations provide the most spatially even sampling pattern across this region. (Note that the scale changes from plot to plot.) Adding 2 more years of data, while tripling the sampling, does not appreciably smooth the pattern at any accumulation period. Further accumulation beyond 4 hours increases the unevenness of the sampling pattern.

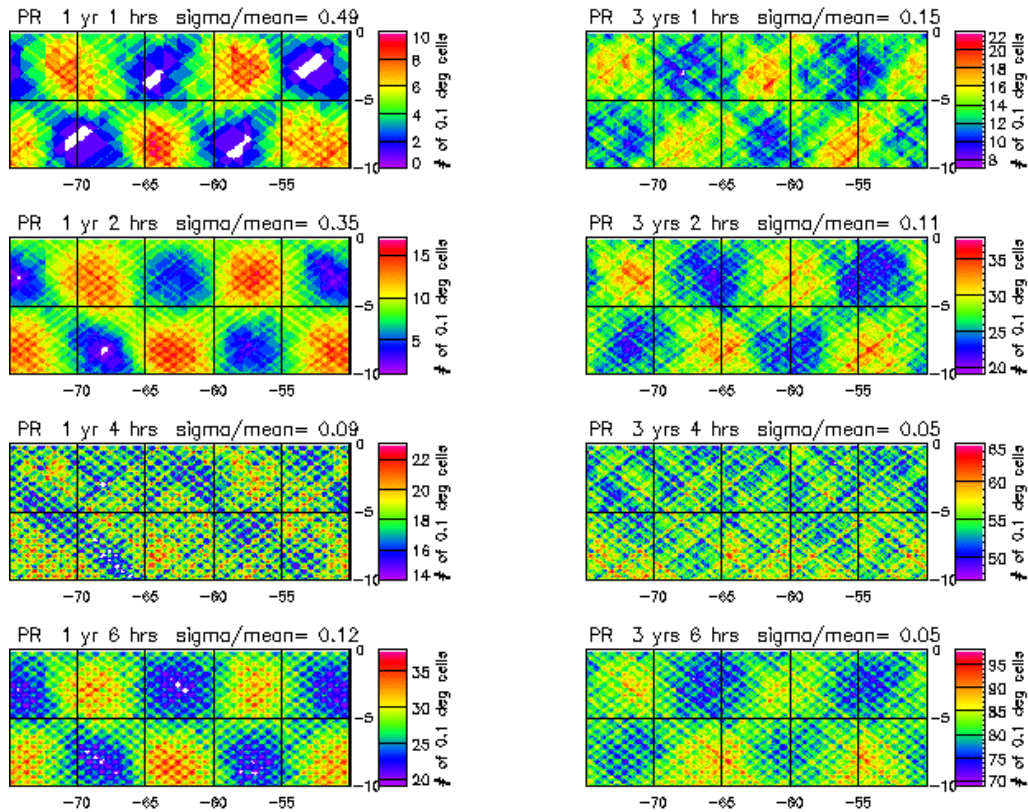


Figure 6-38. Cumulative observed sampling in the Amazon Basin.

**One year (2000)**

**Three years (1998-2000)**

Our study concluded that the optimal time period over which to accumulate the rainfall observations was 4 hours. That interval minimizes the spatial variation and the sampling error across any tropical region. These results are important for our understanding of the hourly variation of rainfall over remote regions such as the Amazon Basin, where conventional observations are not possible. The study also verified its observational results using a simple orbital model and demonstrated the sensitivity of the sampling pattern to the altitude of the TRMM satellite, an important consideration for future missions such as the Global Precipitation Mission.

Andrew J. Negri, Code 912 ([Andrew.J.Negri.1@gsc.nasa.gov](mailto:Andrew.J.Negri.1@gsc.nasa.gov))

On Rainfall Modification by Major Urban Areas: Observations from Spaceborne Rain Radar on TRMM

Most of us have watched local television weather forecasts. Observing the maps closely, we notice that the cities tend to be from 2 to 10 degrees (F) warmer than the surrounding suburbs and rural areas (Figure 6-39). This difference is due to the so-called “urban heat island” effect. Urban areas have numerous buildings, roadways, cars, and artificial surfaces. The heat-retaining properties of these surfaces contribute to the formation of this urban heat island. To understand this effect, think of how uncomfortable it is to walk on hot pavement without shoes. It is estimated that by 2025, 80% of the world’s population will live in cities. As cities continue to grow, urban sprawl creates unique problems related to land use, transportation, agriculture, housing, pollution, and development. Urban expansion also has measurable impacts on the environment.

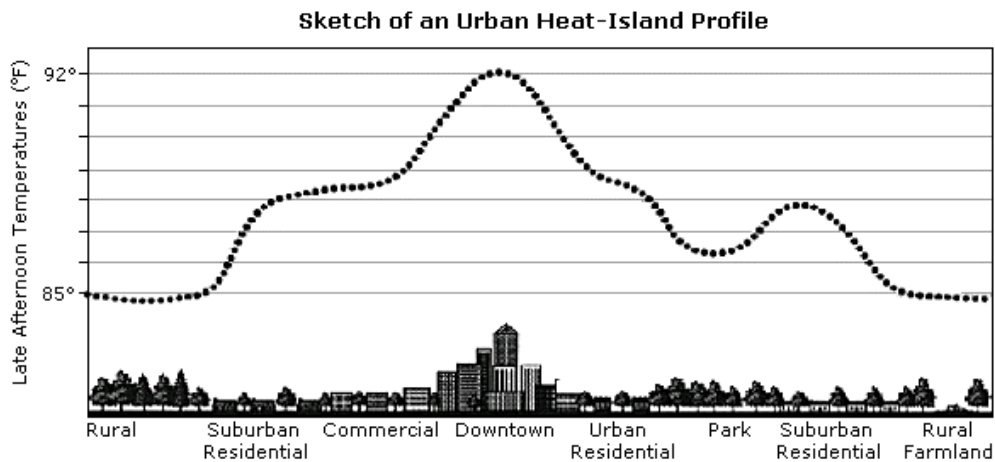


Figure 6-39. Typical Urban Heat Island (UHI) temperature profile (courtesy of The Heat Island Group, LBNL).

In fact, large cities may *create* their own weather and climate. The urban heat island creates a wind circulation that promotes rising air over the city. During the warmer months, researchers have discovered that the rising air can produce clouds or enhance existing ones. Under the right conditions, these clouds can evolve into rain-producers or storms. It is suspected that as air converges due to rougher city surfaces (e.g., buildings) the convergence contributes to the rising air needed to produce rainfall. Converging air forces air upward in the same manner that two colliding cars will be forced upward upon impact. Others have suggested that increased particles in the urban atmosphere from cars and smokestacks contribute to efficient cloud formation. Early studies using ground-based instruments around cities like St. Louis, Chicago, Mexico City, and Atlanta have shown that large cities can affect rainfall over and slightly downwind of metropolitan areas. These studies were limited in many ways, however.

Our recent work represents one of the first published attempts to identify rainfall modification by cities using space-based rain measurements. The work has implications for assessing this anomaly in the water cycle at locations around the globe. The study utilizes the world’s first space-based rain radar aboard NASA’s TRMM satellite. The instrument operates similarly to the Doppler radar seen on evening newscasts. Space-based observations overcome many limitations of ground-based observations and allow for investigation of urban rainfall in numerous cities simultaneously around the world.

This study suggests that major cities in the United States such as Atlanta, Dallas, San Antonio, Austin, and Nashville noticeably affect summer rainfall over and downwind of the urban centers. Our results reveal an average increase of ~28% in monthly rainfall rates within 30–60 km downwind of the metropolis with a modest increase of 5.6% over the metropolis (Figure 6-40.). Portions of the downwind area exhibit increases as high as 51%. The percentage changes are relative to an upwind control area (Figure 6-41.). Our results also show that maximum rainfall rates in the downwind impact area exceeded the mean value in the upwind control area by 48%–116%. The maximum value was generally found at an average distance of 39 km from the edge of the urban center or 64 km from the center of the city. Results are consistent with METROMEX studies of St. Louis almost 2 decades ago and with more recent studies near Atlanta and other cities. Our current research involves utilizing mesoscale models to investigate the impact of urban land surfaces on mesoscale circulations and precipitation.

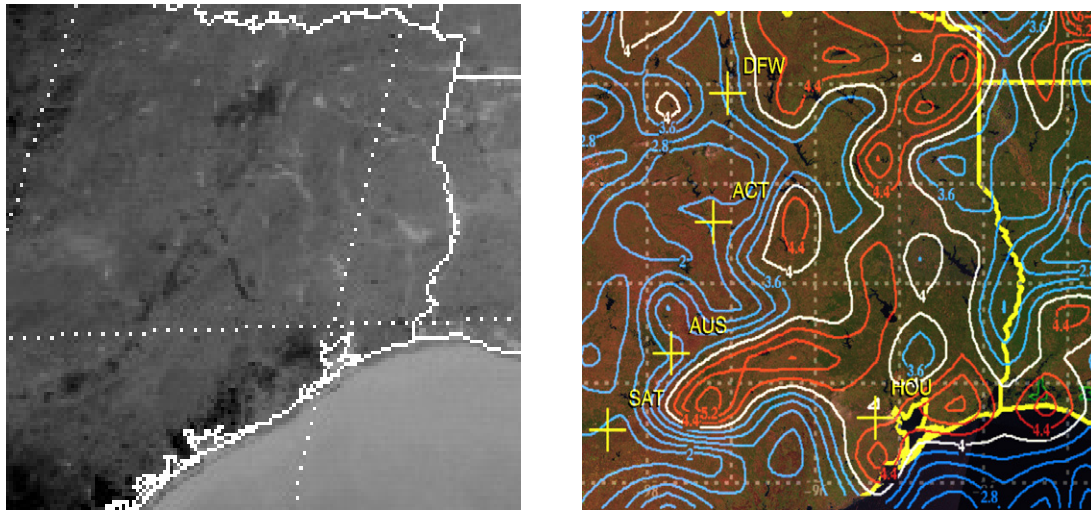


Figure 6-40 left panel is a GOES IR 3.9 micron image of Texas. Urban heat islands for Dallas, Waco, Austin, San Antonio, and Houston are observed as warm, dark regions. Figure 6-40 right panel represents a contour plot of the 3-year, warm season analysis of mean rainfall rates at a height of 2.0 km using the 0.5°-resolution TRMM PR data. The yellow crosses locate the five cities. Values in red are greater than or equal to 4.2 mm/day and demonstrate the increased rainfall downwind of the city heat islands. Values in blue are less than or equal to 3.6 mm/day.

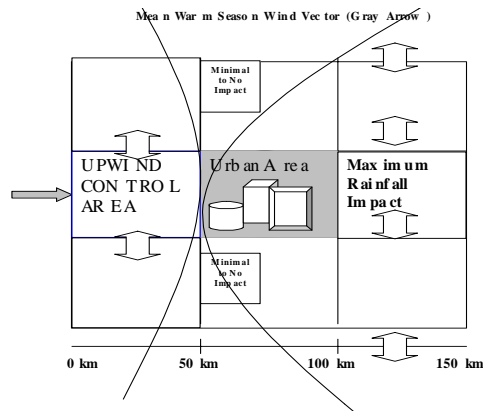


Figure 6-41. Theoretical coordinate system used to define upwind control (UCA), urban, and maximum rainfall impact (MIA) areas. Gray arrow depicts the mean prevailing wind and defines the reference axis for the coordinate system.

This work demonstrates the capability of spaceborne platforms to identify rainfall changes linked to cities and urban sprawl. The research has implications for policymakers, urban planners, water resource managers, and agriculture professionals. Such decision makers may use an understanding of urban rainfall in designing better drainage systems, planning land use, or identifying optimal areas for agricultural activity. Additionally, the results may alert meteorologists that urban surfaces must be considered in the sophisticated computer models that produce weather forecasts. Finally, the study further demonstrates the impact of human development on the environment.

J. Marshall Shepherd, Code 912 ([James.M.Shepherd.1@gscf.nasa.gov](mailto:James.M.Shepherd.1@gscf.nasa.gov))

Cirrus Cloud Microphysical Modeling

The Cirrus Parcel Model Comparison Project (Lin et al., 2002) is an international effort to assess the current understanding of cirrus microphysical modeling. The effort is part of the GEWEX Cloud System Study Working Group on Cirrus Cloud Systems and is led by members of the Mesoscale Atmospheric Processes Branch (Code 912). The project involves the systematic comparison of seven state-of-the-art parcel models of cirrus cloud microphysical initiation and development including aerosol and ice crystal number concentrations and size distributions. Standardized sets of simulations were made for typical cirrus environments. The first set focused on the homogeneous freezing of H<sub>2</sub>SO<sub>4</sub> aerosol particles acting alone as ice nucleating agents, while the second set studied the scenario that both H<sub>2</sub>SO<sub>4</sub> aerosols and heterogeneous ice nuclei were present.

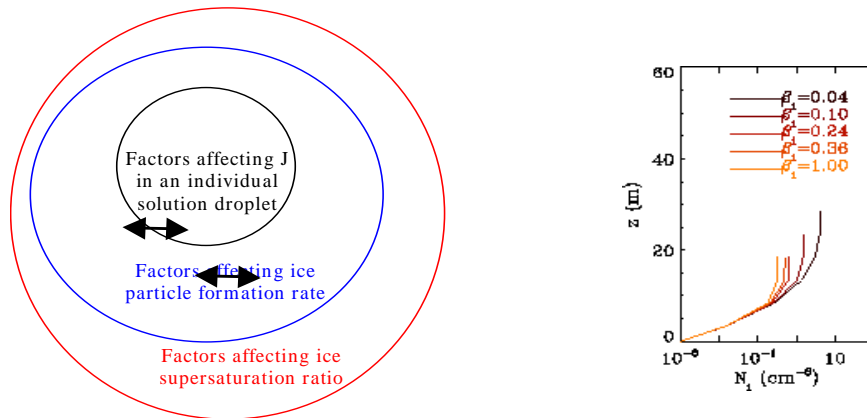


**Figure 6-42. Left: A schematic of the microphysical process interactions. Right: Ice crystal number density as function of height above cloud base during the critical (short) initial ice nucleation period illustrating the strong sensitivity to deposition coefficient,  $\beta_i$ , where the range of values reflects those used in various models. Resultant values of predicted ice particle number concentration,  $N_i$ , range over an order of magnitude and these significant differences persist in the developing simulated cirrus cloud.**

The paucity of knowledge on upper tropospheric (UT) heterogeneous nucleation resulted in major differences in the all-mode nucleation set. We then focused on comparing the homogeneous nucleation simulations. We found qualitative agreement; however, the quantitative disagreements were significant and resulted from a hierarchy of processes that interact and modulate the predicted cirrus microphysical properties. For an aqueous aerosol particle at a given temperature, the homogeneous freezing rate,  $J$ , is rather sensitive to solution concentration. Therefore, aerosol modeling, and formulation of  $J$ , are useful. Moreover, some frequently adopted assumptions in UT aerosol modeling must be modified for application to certain cirrus initiation conditions. For example, attention is needed for the curvature effect (Kelvin's effect), which is ignored in some models, and for the common assumption that the aerosol particles are in environmental equilibrium, which is violated for a parcel lifted by a fast updraft ( $1 \text{ m s}^{-1}$ ) at a cold temperature. Finally, water vapor uptake by nucleated ice crystals controls the maximum ice supersaturation ratio achieved by the parcel, and thus, the duration of active nucleation and the predicted ice particle number concentration. When ice crystals are still small, being just nucleated from aqueous solution, their diffusional growth rates are extremely sensitive to the poorly understood deposition coefficient, which is the probability that a vapor molecule impinging onto the ice surface becomes attached to the surface. The findings highlight the need for laboratory studies on these crucial yet still uncertain parameters.

Ruei-Fong Lin, Code 912/GEST ([Ruei-Fong.Lin.1@gsfc.nasa.gov](mailto:Ruei-Fong.Lin.1@gsfc.nasa.gov))

### Climate Variability and Climate Change

#### Hydrologic Teleconnections during Northern Summer

Atmospheric teleconnection patterns linking continental-scale rainfall anomalies over North America and East Asia have been identified from 4-dimensional assimilated data. These teleconnection patterns appear to arise from intrinsic modes of climate variability linked to intrinsic fluctuations of sea surface temperature (SST) in the extratropical oceans. Two such intrinsic climate models have been identified.

Figure 6-43 shows the patterns of 850-hPa wind, rainfall, and SST associated with the most dominant mode (Mode-1) of U.S. rainfall. Mode-1 explains 32% of the co-variability between U.S. rainfall and 500 hPa geopotential height (not shown) and projects strongly on the disastrous flood over the U.S. midwest in 1993. It depicts a *Pan-Pacific*, zonally oriented rainfall/circulation pattern stretching from east Asia and Japan to North America. We see excessive rainfall over northern and northwestern North America and deficient rainfall over the eastern and southeastern U.S. The rainfall pattern is coupled to an anomalous low-level anticyclonic flow over the eastern U.S., which favors the transport of warm moist air from the Gulf coast to the midwest and dry air along the east coast. The band of excessive rainfall linking Canada and Japan coincides with regions of low-level cyclonic flow. Along the equator, we see a weaker signal indicating generally enhanced rainfall in a large fetch of enhanced westerlies in the central and eastern equatorial Pacific. The regressed SST anomaly pattern for Mode-1 (Figure 6-43b) suggests possible El Niño influence, as evident in the positive SST over the equatorial eastern and central Pacific. A prominent feature in the Figure 6-43b is the presence of an extensive area of below-normal SST in the extratropical Pacific (near  $40^\circ\text{N}$ ), coinciding with anomalous low-level westerlies and enhanced rainfall. These features suggest the importance of extratropical air-sea interaction in sustaining Mode-1.

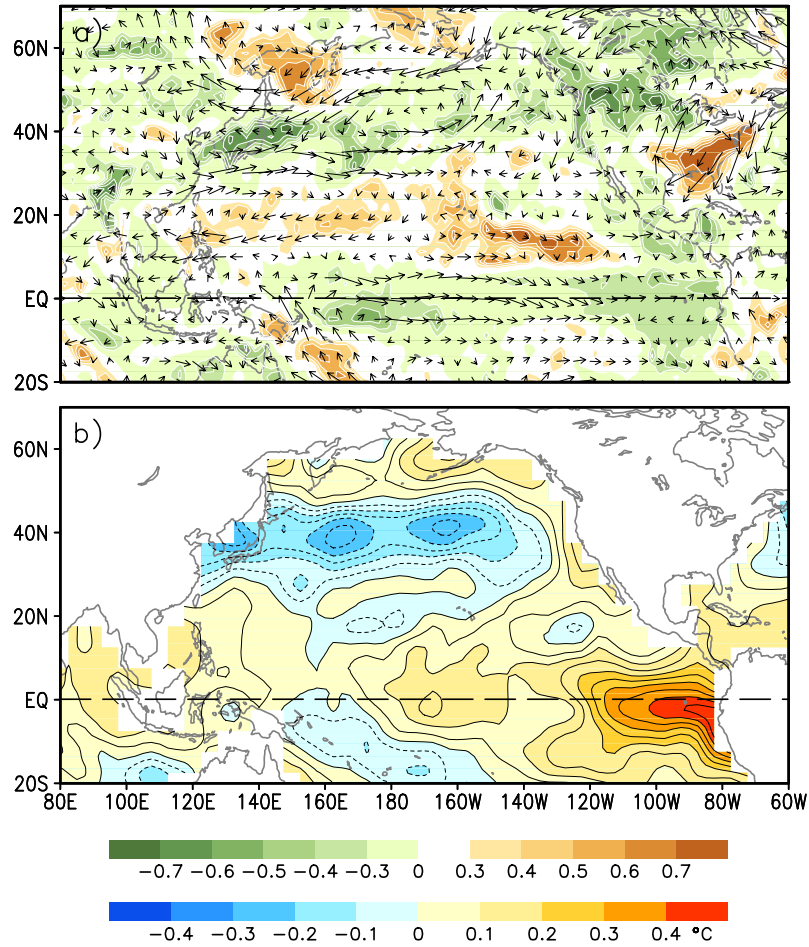
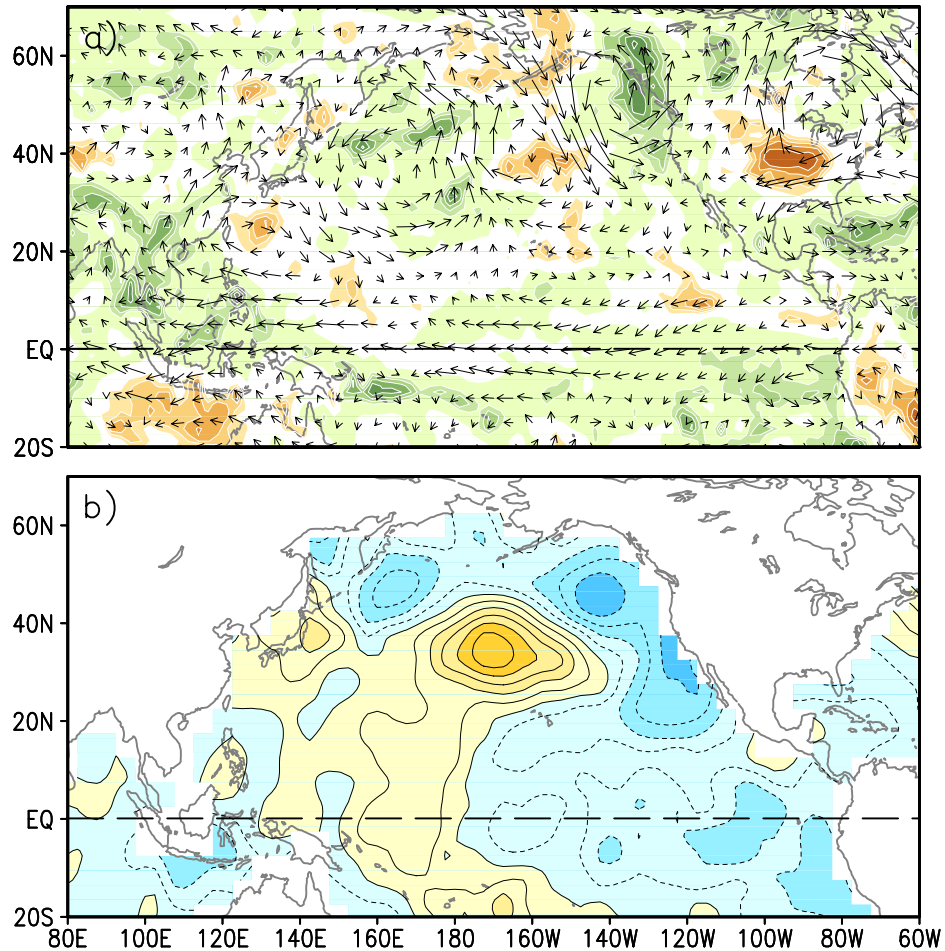


Figure 6-43. Spatial patterns of 850-hPa horizontal wind, CMAP rainfall, and SST anomalies related to Mode-1. (a) Regressed wind anomaly for the period of 1955-98. Correlation between PC1r and CMAP rainfall anomaly for the period of 1979-98 is shaded. (Green areas with negative correlation are above normal.). (b) Regressed SST anomaly for the period of 1955-98 (contour interval: 0.05°C).

Mode-2 explains 30% of the co-variability between U.S. rainfall and global geopotential height. The associated 850-hPa wind and CMAP rainfall patterns suggest that U.S. summer rainfall variability may be associated with deep convection (heavy monsoon rainfall) in the IndoChina and western Pacific region (Figure 6-44a). The principal components (not shown) of this mode show a strong projection on the 1988 drought over the U.S. We see excessive rainfall over the west coast of Canada and below normal rainfall over the Great Plains and midwest. The associated low-level flow indicates a large anticyclone over northeastern North America coupled to a cyclone over the Gulf region. This anticyclone/cyclone couplet induces anomalous low-level easterlies in southern U.S. These easterlies effectively cut off the supply of moisture from the Gulf of Mexico, resulting in below-normal rainfall in the Midwest. A well-developed cyclonic circulation over northwestern North America, with southerly flow that feeds moist oceanic air into the region, may be responsible for the excessive rainfall along the west coast of Canada (Figure 6-44a). The continental wave pattern over North America appears to be a part of a much larger and well-organized wavetrain emanating from the subtropical western Pacific, in an arc across the north Pacific to North America. Regions of enhanced (reduced) rainfall appear to align along the direction of the wavetrain, coinciding with low-level cyclonic (anticyclonic) circulation that can be traced back to enhanced convection over Indo-China. The anticyclone over the subtropical western Pacific near the Philippines is of particular interest, because this circulation feature has been identified as one of the key features of the Asian summer monsoon variability affecting droughts and floods in China, Japan, and Korea (Lau et al. 2000). Mode-2 is associated with substantial changes in extratropical SST, with positive (negative) SST anomalies underlying the anticyclones (cyclones) (Figure 6-44b), suggesting that the atmospheric circulation pattern may be anchored in place by the SST anomalies. Since there is no significant SST signal in the tropical eastern Pacific, Mode-2 appears to be independent of El Niño/La Niña, but rather may have stemmed from fluctuations of heat sources and sinks associated with the Asian/West Pacific monsoon convection.



**Figure 6-44.** Same as Figure 6-43, except for Mode-2.

Lau, K.M. and H.T. Wu, 2001: Intrinsic modes of coupled rainfall/SST variability for the Asian summer monsoon: a re-assessment of monsoon-ENSO relationship. *J. Climate*, **14**, 2880-2895.

Lau, K.M. and H. Weng, 2000: Teleconnection linking summertime rainfall variability over North America and East Asia. *CLIVAR Exchanges*, **5**, 18-20.

William K.M. Lau, Code 913 ([William.K.Lau.1@gsfc.nasa.gov](mailto:William.K.Lau.1@gsfc.nasa.gov))

Cloud, SST, and Climate Sensitivity Inferred from Satellite Radiance Measurements

High-level clouds have a significant impact on the radiation energy budgets and, hence, the climate of the Earth. Convective cloud systems, which are controlled by large-scale thermal and dynamical conditions, propagate rapidly within days (Figure 6-45). These cloud systems propagate over oceanic regions with spatially varying sea surface temperature (Figure 6-46).

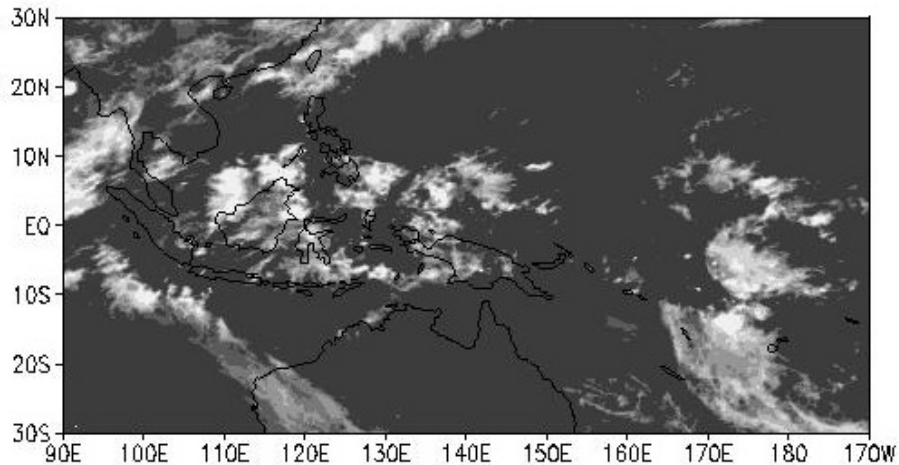


**Figure 6-45. GMS satellite imagery showing the cloud clusters in the tropical western Pacific. Propagation of cloud systems is primarily in the zonal direction.**

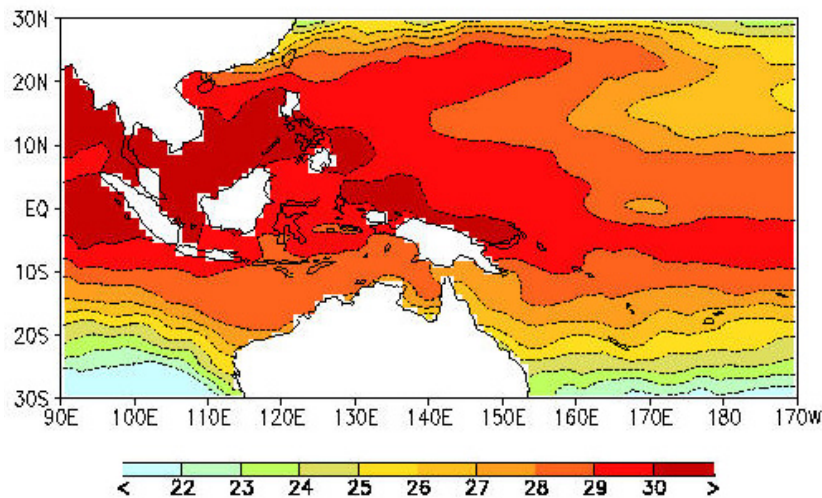


**Figure 6-46. The weekly-mean sea surface temperature distribution for the period 7-13 June 1998 taken from NCEP data archive.**

We use the radiances measured by Japan's Geostationary Meteorological Satellite (GMS) to study the response of high-level cirrus clouds to the sea surface temperature (SST) in the tropical western and central Pacific (30S–30N; 130E–170W), where the ocean is warm, and deep convection is intensive. Twenty months (January 1998–August 1999) of GMS data are used, which cover the second half of the strong 1997–1998 El Niño.

When deep convection moves to regions of high SST, the domain-averaged high-level cloud amount decreases. A +2 °C change of SST in cloudy regions results in a relative change of –30% in high-level cloud amount (Figure 6-47). Figure 6-48 shows that the amount of cirrus anvil clouds relative to the convection core decreases as the SST increases. The decrease in cloud amount is due to the reduced cumulus detrainment associated with an increase in precipitation efficiency when temperature is high. This large change in cloud amount is due to clouds moving through oceanic regions with varying SST.

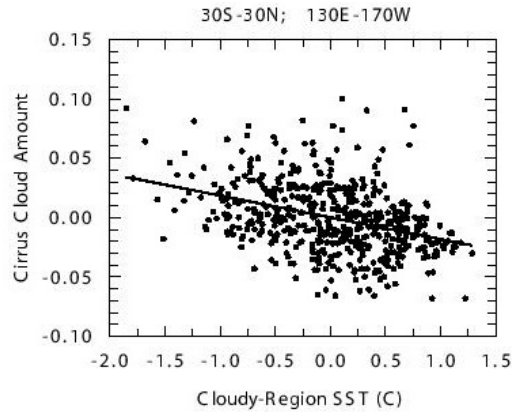


**Figure 6-47. The relation between high-level clouds and the SST.**

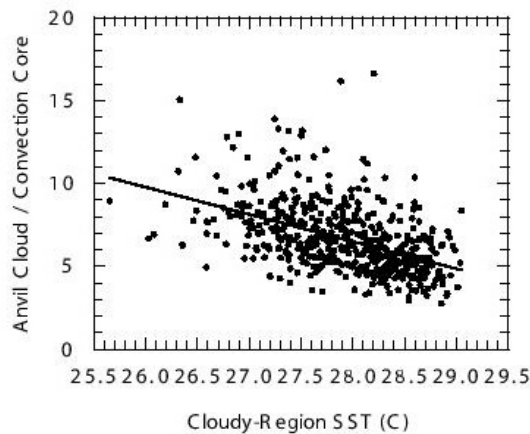


**Figure 6-48. Relation between the SST and the ratio of the area of cirrus anvils to that of convection cores.**

A reduction in high-level cloud amount in the equatorial region implies a drier upper troposphere in the off-equatorial region, and the greenhouse warming of high clouds and water vapor is reduced through enhanced longwave cooling to space. The results are important for understanding the physical processes relating SST, convection, and water vapor in the tropics. They are also important for validating climate simulations using global general circulation models.

Ming-Dah Chou, Code 913 ([Ming-Dah.Chou.1@gsfc.nasa.gov](mailto:Ming-Dah.Chou.1@gsfc.nasa.gov))

#### Global Warming: Evidence from Satellite Observations

Meteorological measurements of air temperature over land, taken about a meter above the ground, and ocean surface temperature are commonly used in estimating global temperature and its long-term trend (e.g., Hansen et al., 1996, and Jones et al., 1999). However, since these conventional data represent point values (i.e., not spatial averages), they may overemphasize adverse effects due to urbanization (Hansen et al., 1999), land use, and deforestation.

Observations made by the Microwave Sounding Unit (MSU) radiometer on board NOAA operational polar-orbiting satellites represent averages over radiometer footprints, each of which has an area of about  $10^4 \text{ km}^2$ . Also, MSU data coverage is uniform over land and ocean. For these reasons, satellite data are potentially valuable in monitoring global temperature.

In a pioneering study, Spencer and Christy (1990) used the measurements made by the MSU radiometer in Channel 2 (Ch 2), centered over a narrow spectral interval near 53.74 GHz of the oxygen absorption band, to determine global temperature trend. Each Ch 2 observation reflects the vertically weighted mean temperature of the atmosphere, with a peak weight near the midtroposphere, and is highly correlated with the surface temperature. However, problems in creating the MSU Ch 2 global temperature time series, mainly due to instrument calibration errors introduced by slow satellite orbital drift over several years, have not been accounted for satisfactorily by these authors. We have developed an innovative technique to remove these errors with the help of the warm blackbody temperature data, which is used in calibrating the MSU.

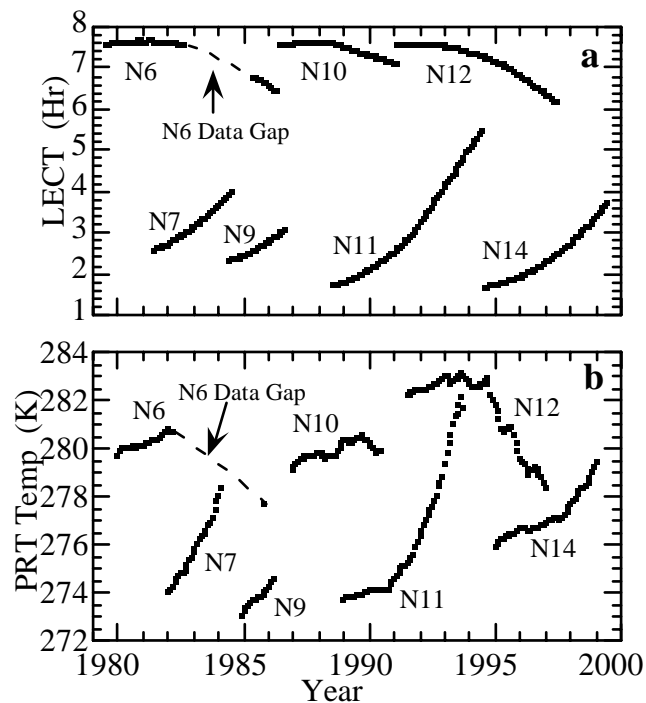


**Figure 6-49. a) Temporal change in Local Equatorial Crossing Time (LECT) of each satellite, b) Temporal change in 12-month running-mean warm blackbody temperature of each satellite.**

In Figure 6-49a, we show the manner in which the *morning* satellites (NOAA 6, 10, and 12) and *afternoon* satellites (NOAA 7, 9, 11, and 14) drift in Local Equatorial Crossing Time (LECT) over a period of several years. Similarly, in Figure 6-49b, we show that the 12-month running-mean of warm blackbody temperature changes gradually by a small amount ( $< 10 \text{ K}$ ) due to drift in LECT over the same time period. From these figures, it is clear that the warm blackbody temperature for the *morning* satellites ultimately decreases following the LECT. On the other hand, the warm blackbody temperature of the *afternoon* satellites steadily increases with time following the LECT. This time-dependence of the warm blackbody temperature is the key to our MSU Ch 2 calibration correction scheme.

When observations from two successive satellites overlap over an extended period of time (see Figure 6-49a), we expect that the 12-month running-mean of Ch 2 temperature from these satellites should track one another with only a constant calibration offset. If this offset is not constant during the overlap period, we infer it is because of the calibration errors. In the analysis of MSU data made by Prabhakara et al. (2000), this calibration error is quantified with the help of the 12-month running-mean warm blackbody temperature that is shown in Figure 6-49b.

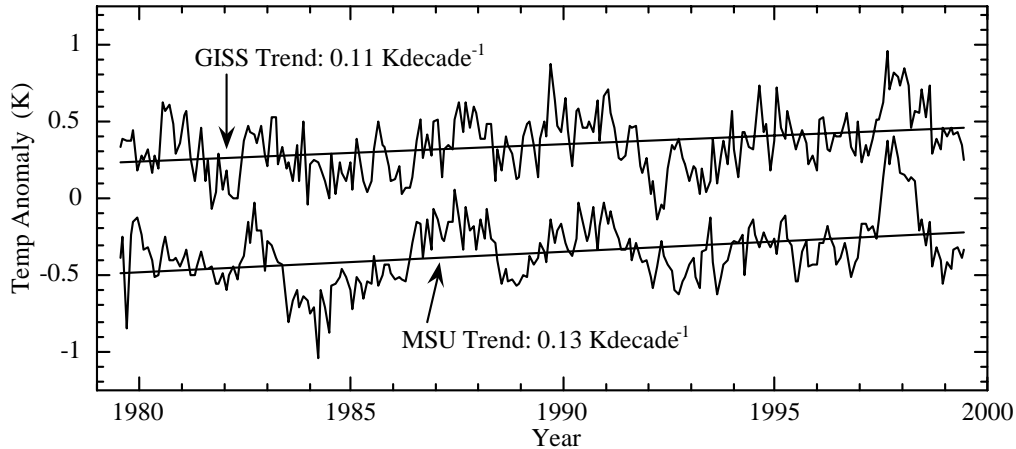


**Figure 6-50. Anomaly time series and trend of MSU Ch 2 global monthly-mean temperature for the time period 1980 to 1999 is compared with corresponding information deduced from the conventional data analysis made by GISS. Note for clarity that the MSU and GISS time series are offset by 0.7 K.**

In Figure 6-50, we show the monthly-mean MSU Ch 2 temperature anomaly time series after correcting for calibration errors. From this time series, we find that the vertically weighted global-mean temperature of the atmosphere, with a peak weight near the midtroposphere, increased by 0.13 K/decade during the period 1980 to 1999.

We estimate the total error in the global temperature trend to be 0.05 K/decade. This error includes uncertainties in the overlap adjustment between NOAA 9 and 10, and our procedure to improve the calibration. It also includes errors introduced by variations of hydrometeors in the atmosphere and surface emissivity. With this error, the MSU estimate of the global temperature trend is  $0.13 \pm 0.05$  K/decade.

In Figure 6-50, we also show the surface temperature anomaly time series deduced by Goddard Institute for Space Studies (GISS) from conventional data corrected for urbanization effects (see Hansen et al., 1999). This time-series, also presented in Prabhakara et al. (2000), has a trend of 0.11 K/decade. The two time series shown in Fig. 6-50 have similar interannual variability. From this analysis, we find the global warming estimated from conventional meteorological data that have been corrected for urbanization effects is in reasonable accord with the satellite-deduced result. This demonstrates the potential of the satellite data to monitor the global temperature.

Hansen, J., R. Ruedy, M. Sato, and R. Reynolds, 1996: Global surface air temperature in 1995: Return to pre-Pinatubo levels. *Geophys. Res. Lett.*, **23**, 1665-1668, 1996.

Hansen J., R. Ruedy, J. Glascoe, and M. Sato, 1999: GISS analysis of surface temperature change. *J. Geophys. Res.*, **104**, 30997-31022. (For more information, visit <http://www.giss.nasa.gov/data/update/gistemp/GLB.Ts.txt>)

Jones, P.D., M. New, D.E. Parker, S. Martin, and I.G. Rigor, 1999: Surface air temperature and its change over the past 150 years. *Rev. Geophys.*, **37**, 173-199.

Prabhakara, C., R. Iacovazzi, Jr., J.-M. Yoo, and G. Dalu, 2000: Global warming: Evidence from satellite observations. *Geophys. Res. Lett.*, **27**, 3517-3520.

Spencer, R.W. and J.R. Christy, 1990: Precise monitoring of global temperature trends from satellites. *Science*, **247**, 1558-1562.

Prabhakara, C. and R. Iacovazzi, Jr., Code 913 ([Prabhakara.Cuddapah.1@gsfc.nasa.gov](mailto:Prabhakara.Cuddapah.1@gsfc.nasa.gov))